Microscopy and Microanalysis (2021), 1–7
doi:10.1017/S1431927621000441

Microscopy AND Microanalysis

Original Article

Direct Visualization of the Earliest Stages of Crystallization

Manish Kumar Singh[1*a], Chanchal Ghosh[1*a], Benjamin Miller[2*a] and C. Barry Carter[3,4]

[1]Department of Materials Science and Engineering, University of Connecticut, Storrs, CT 06269, USA; [2]Gatan Inc., 5794 W. Las Positas Blvd, Pleasanton, CA 94588, USA; [3]Department of Chemical and Biomolecular Engineering, University of Connecticut, Storrs, CT 06269, USA and [4]Center for Integrated Nanotechnologies, Sandia National Laboratories, Albuquerque, NM 87185, USA

Abstract

Investigating the earliest stages of crystallization requires the transmission electron microscope (TEM) and is particularly challenging for materials which can be affected by the electron beam. Typically, when imaging at magnifications high enough to observe local crystallinity, the electron beam's current density must be high to produce adequate image contrast. Yet, minimizing the electron dose is necessary to reduce the changes caused by the beam. With the advent of a sensitive, high-speed, direct-detection camera for a TEM that is corrected for spherical aberration, it is possible to probe the early stages of crystallization at the atomic scale. High-quality images with low contrast can now be analyzed using new computing methods. In the present paper, this approach is illustrated for crystallization in a $Ge_2Sb_2Te_5$ (GST-225) phase-change material which can undergo particularly rapid phase transformations and is sensitive to the electron beam. A thin (20 nm) film of GST-225 has been directly imaged in the TEM and the low-dose images processed using Python scripting to extract details of the nanoscale nuclei. Quantitative analysis of the processed images in a video sequence also allows the growth of such nuclei to be followed.

Key words: beam-sensitive, crystallization, $Ge_2Sb_2Te_5$, low-dose, Python scripting

(Received 13 December 2020; revised 15 April 2021; accepted 27 April 2021)

Introduction

Understanding the early stages of nucleation and growth of crystalline grains is of immense importance for understanding many phenomena, including phase transformations and crystal growth (Gao et al., 2019; Ogata et al., 2020). Efforts have been made to address these issues, thanks to the emergence of new improved instruments having capabilities to resolve the sub-angstrom features in the specimen (Carter & Williams, 2016). Computer modeling has also contributed significantly to predicting the nucleation and subsequent growth of crystalline grains. Coupling modern experimental techniques and computational strategies should, in principle, provide the capability to uncover the underlying questions. For example, in transmission electron microscope (TEM), if well-defined lattice, and/or interatomic, spacings can be probed with a high signal-to-noise ratio (SNR), then evolution during the early stages of nucleation can be followed (Li et al., 2019). However, the structural evolution at the nanometer scale in most materials is inherently unstable when the material is irradiated, in particular by an electron beam (Zhu et al., 2017; Zhang et al., 2018; Nam et al., 2019; Murthy et al., 2020). One way to tackle this challenge experimentally is by using a low electron-dose to acquire an image with atomic resolution using a high-speed camera (McMullan et al., 2009; Miller et al., 2019). This strategy helps to record changes at the nanoscale before the beam can alter the original state of the material. However, the contrast of each image is reduced to a level where it becomes almost indistinguishable to the eye, despite its containing the desired information. Newer strategies are then needed to process the image while retaining the scientific information and making the image details interpretable (Bustillo et al., 2016; Panova et al., 2019).

Phase-change materials are important for their usage in nonvolatile, phase-change memory (PCM) devices. The underlying principle of a PCM device is based on a large change in optical reflectivity or electrical conductivity when materials undergo a phase transformation from the amorphous to crystalline state (Wuttig & Yamada, 2007; Raoux, 2009). $Ge_2Sb_2Te_5$ (GST-225) is one such PCM; it has been examined extensively due to its optimal amorphous to crystalline transformation temperature, the speed of transformation, and good thermal stability in the amorphous state. Crystallization in capped GST-225 thin films (ca. 100 nm) has been observed at 170°C: the amorphous material transformed to a metastable face-centered cubic phase (Yamada et al., 1991). The crystallization is also influenced by the heating rate; it has been reported that below a heating rate of 0.6°C/s, the activation energy barrier will be too high for crystallization to take place (Choi et al., 2009).

The process of crystallization proceeds by homogeneous nucleation in the amorphous matrix. The uncapped films are susceptible to surface oxidation and crystallize at a somewhat lower temperature (~150°C). This lower crystallization temperature has been ascribed to heterogeneous nucleation near-surface regions in the films (Noé et al., 2016). A GST-225 film of thickness 10 nm, exposed to atmosphere, can completely crystallize even at room temperature (RT) (Kooi et al., 2004). However, capped films

***Authors for correspondence**: Manish Kumar Singh, E-mail: manish.singh@uconn.edu; Chanchal Ghosh, E-mail: chanchal.ghosh@uconn.edu and Benjamin Miller, E-mail: Benjamin.Miller@ametek.com

[a]Manish Kumar Singh, Chanchal Ghosh, and Benjamin Miller equally contributed to the present study and can be regarded, therefore, as being main authors.

Cite this article: Singh MK, Ghosh C, Miller B, Carter CB (2021) Direct Visualization of the Earliest Stages of Crystallization. *Microsc Microanal*. doi:10.1017/S1431927621000441

(less than 10 nm in thickness) exhibit a delayed crystallization, which is attributed to stresses induced by capping layers on the film (Simpson et al., 2010). There are limited reports related to the effect of oxidation on the crystallization behavior. The chemistry of the transformed phase has been established to be the same as that of the parent phase (Song et al., 2008), which further diminishes the contrast in the recorded image.

An added complication for GST-225 is its sensitivity to the electron-dose which induces the phase change even in the absence of thermal stimulus (Tripathi et al., 2018; Jiang et al., 2019). This "beam damage" occurs at all dose rates. However, minimizing the electron-dose can delay the beam-induced changes.

Investigations have been carried out using electron-dose rates between 10^3 and 10^4 e/A^2/s. This dose rate is consistent with typical high-resolution TEM (HRTEM) imaging experiments. The current work deals with several orders of magnitude lower dose rate than is typical for HRTEM. For a typical (HR)TEM, electron-dose rate of 11,000 e/A^2/s induces structural changes in GST within 10 min (Jiang et al., 2020). GST material can be amorphized or crystallized depending on the dose rate: a dose rate of 6,000 e/A^2/s can crystallize the sample, while a dose rate of 11,000 e/A^2/s would cause amorphization (Jiang et al., 2019). The investigation of the phase transformation in GST-225, therefore, is a challenging issue and requires newer ways to enhance the contrast and visibility especially at the nanometer scale (Panova et al., 2019).

This paper reports an *in situ* investigation of the initial stages of nucleation and growth during the amorphous to crystalline transformation in an uncapped GST-225 film at the atomic scale by using a low electron-dose. The lattice information recorded in the TEM image is difficult for a human observer to see due to the low SNR and large size of the image frames but is revealed by a custom-written script in Python. This strategy may be adopted for a broad range of beam-sensitive materials at different stages of transformation.

Materials and Methods

The GST-225 film (~20 nm thick) was sputtered onto the SiN_x support film of a microelectromechanical system (MEMS)-based chip without a capping layer for *in situ* investigation using aberration-corrected environmental TEM (Tripathi et al., 2020). The film was heated *in situ* from RT to 140°C at a rate of 5°C/s using an Aduro 300 TEM holder. The dynamics of the structural transformation have been recorded, using a low electron-dose (6.67 e/Å^2/s), a large-field-of-view, and a high-speed direct-detection camera (Gatan K3 IS).

A Python script run within Digital Micrograph was used to process the *in situ* video dataset recorded using the K3 IS camera to produce a map of lattice-spacing, orientation, and visibility, from individual frames in the dataset. These maps are based on fast Fourier transforms (FFTs) of sub-regions and are displayed in color, where the hue corresponds to the direction of the strongest lattice-spacing peak in the diffractogram, and the brightness corresponds to the intensity of this peak. Since the Python script runs within Digital Micrograph, no data conversion is needed to process the raw data, and the result can be quickly visualized in the same software that was used to collect the raw data. The algorithm of the Python script has been summarized in the following.

First, a set of windows was defined where each window has size $N \times N$ and spacing $M \times M$. Generally, M should be smaller than N, so that the windows have significant overlap. Here, $N = 128$ and $M = 32$ for images with a total size of 5,760 × 4,092 px. The next step is to reshape the data into a virtual four-dimensional (4D) cube, and then compute the two-dimensional (2D) FFT over two dimensions of this cube. This produces a dataset similar to the 4D cubes of 4D-scanning TEM (STEM) experiments, but with diffractograms of each $N \times N$ window, rather than diffraction patterns. Then, each $N \times N$ diffractogram is transformed to polar coordinates and the maximum is taken across the radial dimension to create a one-dimensional (1D) profile (azimuthal dimension). For each 1D profile, the maximum is found (along the azimuthal dimension), and both the position (angle) and intensity of this maximum are recorded as single pixels in corresponding maps. The azimuthal angle map is then assigned a color scale, and the resulting RGB map is multiplied by the intensity-value map. The maps are finally displayed in Digital Micrograph with the magnification calibration based on the original magnification and the spacing M.

The principal steps of the image processing are illustrated in Figure 1. Figure 1a shows the as-recorded image using K3 IS, and the corresponding virtual 4D-STEM data cube and color map are depicted in Figures 1b and 1c, respectively. The diffractogram embedded in Figure 1b corresponding to a region of interest (ROI) is also shown; it is color-coded region (blue), which is highlighted in Figure 1c.

While the maps produced in this way are similar to orientation maps, they are not true depictions of crystalline orientation since they only measure the direction and intensity of a single peak in the diffractogram of each $N \times N$ region. The algorithm is simple and ignores all the other spots in each pattern. This means that all regions with the exact same orientation will be the same color. Thus, the maps are useful for measuring the size of single-crystal regions. Two regions in the map could have very different orientations but still be assigned the same color if the brightest spot in the two patterns happened to be the same. Nonetheless, it is statistically unlikely that two regions with different orientations would have the same brightest lattice spot and contact each other, making these maps suitable for measuring crystallite size, but not crystallite orientation.

Results and Discussion

Several low-dose micrographs of the nucleation and growth dynamics of GST-225 films as a function of temperature are depicted in Figure 2. Figures 2a–2f show the phase and structural morphology of the film at the temperatures corresponding to 25 (RT), 30, 35, 40, 45, and 50°C, respectively. The power spectra corresponding to the frames in Figures 2a–2c are shown in Figures 2g–2i. The SNR in the low-dose images is quite small, that is, the contrast from the films is quite weak, making it difficult to distinguish the crystalline regions by eye. However, the corresponding power spectra confirm the presence of ordered domains in the images which are essentially the nucleated crystallites at a very early stage of growth. At the initiation of the nucleation event, as confirmed by the presence of a few pairs of low-intensity spots in the power spectra, the initial crystallites are quite small, and the density of the nuclei is low. One such pair of spots correspond to 111 planes of *fcc* GST-225 is marked in Figure 2h. However, with the increase in temperature, the crystallites size increases as does the density of crystallites. These increases are clearly reflected in the corresponding power spectra, where the intensity and the number of the lattice spots increase with the increase in the temperature. Extracting contrast usually is challenging for images obtained at low electron doses; it is even more so in the present set of micrographs showing the early stages of the nucleation. Bragg filtering using the diffraction spots does not

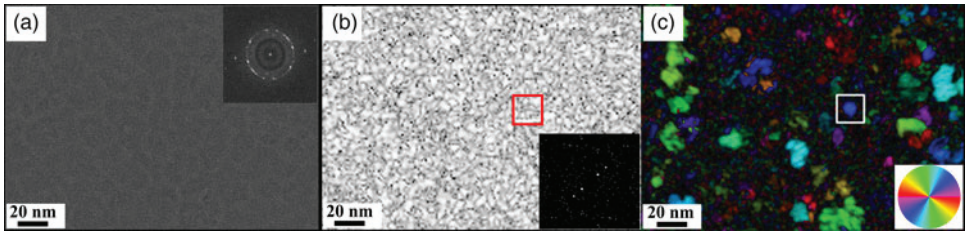

Fig. 1. Presentation of major steps followed in processing of image using Python scripting. A low-dose image of GST-225 heated at 140°C with FFT as inset (**a**), corresponding computed 4D data cube (similar to 4D-STEM data cube) with embedded diffractogram of ROI (**b**), and color-coded image obtained after Python scripting within Digital Micrograph (**c**).

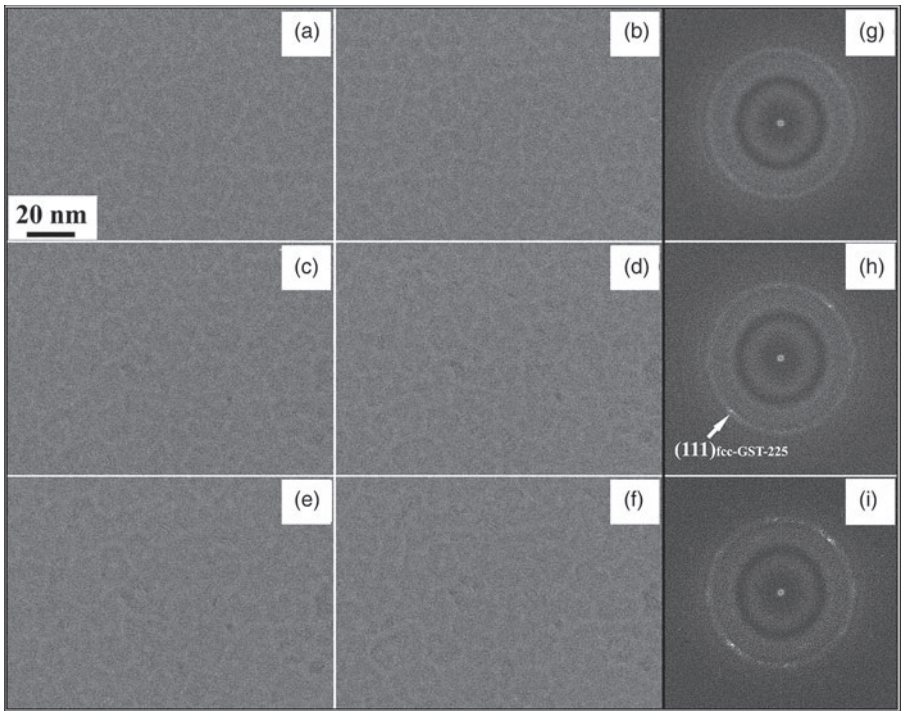

Fig. 2. Structural evolution of GST-225 at (**a**) RT, (**b**) 30°C, (**c**) 35°C, (**d**) 40°C, (**e**) 45°C, and (**f**) 50°C. Power spectra corresponding to (**a–c**) are shown in (**g–i**), respectively. Reflection corresponding to (111) plane of GST-225 is depicted in (**h**), showing the onset of crystallization at 30°C.

help much in the current scenario because in the early stages of nucleation, the very small domain sizes of the crystallites provide very little contrast relative to the background even in filtered micrographs.

The strategy adopted to enhance the contrast and visibility at the early stages of crystallization is illustrated in Figure 3. The algorithm not only enhances the contrast but is also sensitive to the orientation of crystals. Figure 3a shows the as-recorded low-dose image of GST-225 at ~140°C and six ROIs of 128 × 128 px (128 px equals 4.69 nm) depicted as 1, 2, 3, 4, 5, and 6. The important point is that the entire image is automatically scanned and that the "resolution" is determined by the chosen ROI. Power spectra corresponding to each ROI (1–6) showing the brightest pair of spots is also displayed. The orientation of the spots in the power spectra 1, 2, 3, and 4 is clearly different and is mapped in different colors (yellow, magenta, blue, and pink) as shown in the Python-processed image (Fig. 3b). The spot orientations in 1 and 5 and 4 and 6 are very close and therefore, lead to very similar colors. The emergence of spots in different orientations suggests that crystallization in GST-225 is random in nature.

Contrast enhancement of the low-dose images shown in Figures 2a–2f was carried out using the newly developed Python script, described in the "Materials and Methods" section; the processed images are shown in Figures 4a–4f. The crystallized grains are displayed in different colors where similarly colored crystallites correspond to the same brightest spot in their respective power spectrum. These processed images can be considered pseudo-orientation maps (described in the "Materials and Methods" section), where grains with similar Bragg diffracted planes are represented with similar colors. The processed micrographs displaying the early stages of crystallization events at the 25 (RT), 30, 35, 40, 45, and 50°C are depicted in Figures 4a–4f, respectively. The development of GST-225 crystallites is clearly observed in the processed image recorded at RT; such observations would be uncertain in the as-recorded micrograph. Crystallization at RT can be attributed to the aging of the uncapped film in ambient conditions. Moreover, all the regions of the sample did not transform concurrently as the appearance of newly formed crystallites can be observed in all the processed micrographs.

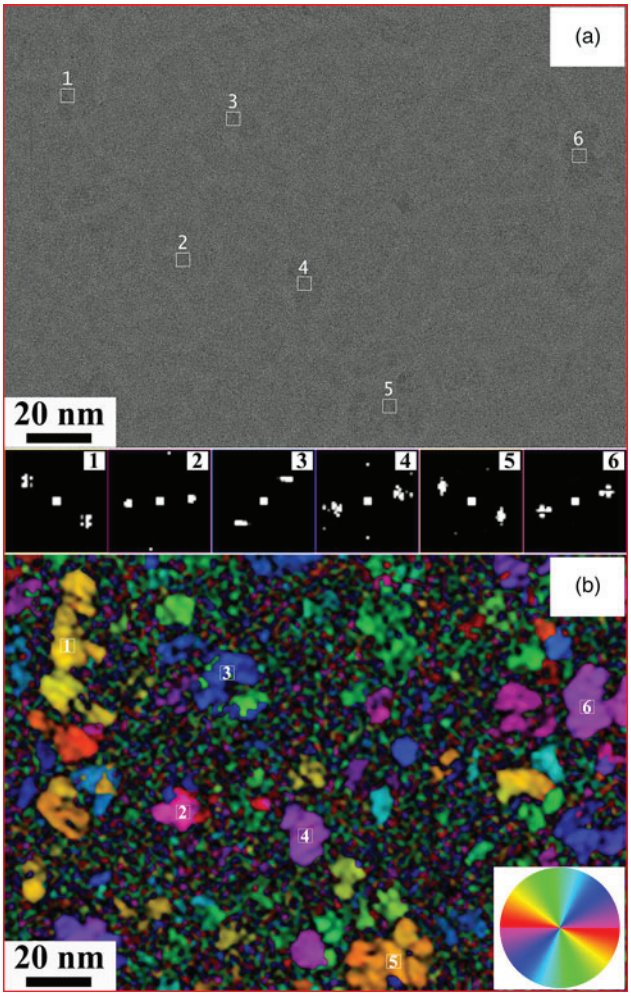

Fig. 3. Illustration of the scripting scheme adopted for contrast enhancement and visibility. A low-dose image of GST-225 heated at 140°C showing ROIs numbered 1–6 of 128 × 128 px and their respective power spectra (**a**) and the corresponding processed image using Python scripting within Digital Micrograph (**b**).

The growth behavior of the individual crystals can be tracked, as shown by arrows in the collage of processed micrographs. Initially, the growth rate is observed to be quite high (up to 40°C), but eventually, the size of the crystallites saturates with the increase in temperature. The crystallites are seen to follow a bimodal trend in their size distribution: two different sizes of crystallites can be readily observed. Another interesting observation from the current set of micrographs is that growing crystals with related orientations merge together giving an oriented attachment. As might be anticipated, the nucleation of one particular type of oriented crystallite promotes the nucleation of similarly oriented nuclei nearby which minimize the total energy of the system through the generation of coherent interfaces. This behavior is not observed for all the crystallites seen in the micrographs, but develops once the nuclei attain a critical size where the volume energy exceeds the surface energy. The growth of a few crystallites is also tracked in the micrographs and marked with white arrows. In the initial frames, the crystallites size increases quickly but saturates once the temperature increased above 40°C. In the present study, the nucleation of GST-225 is predominately heterogeneous, consistent with the appearance of crystals at very low temperatures. The uncapped film was exposed to the atmosphere for longer time leading to surface oxidation, which can provide the heterogeneous nucleation sites. Moreover, owing to the island morphology of the film, the inter-island boundaries can also act as the additional sites for the heterogeneous nucleation.

It is important to note that the appearance of random, small, colored dots in the background does not indicate crystallization; the power spectrum exhibits continuously changing intensity and random orientation of the smallest spots. In the present *in situ* video dataset, if the color of these small spots changes from one frame to the next, it can assumed that these random, background, color dots are not actually indicating crystallites. This is one of the major benefits of continuously capturing *in situ* video data, rather than individual snap-shot images. In the processed images, continuous change in the background-colored dots around a grown crystal marked with white circles in Figures 4a–4c is illustrated as insets of digitally magnified ROIs. The current observation suggests that the fine-colored dots are noise and are not crystalline regions.

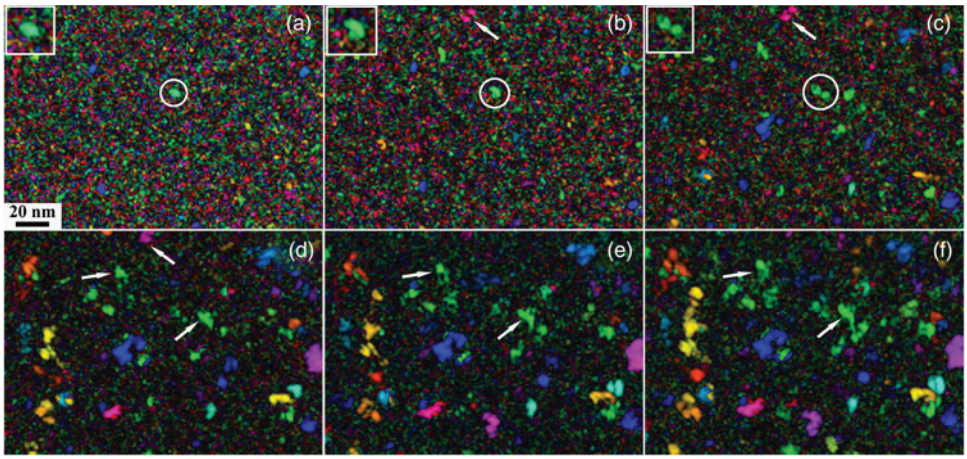

Fig. 4. Depiction of crystallization in GST-225 at (**a**) RT, (**b**) 30°C, (**c**) 35°C, (**d**) 40°C, (**e**) 45°C, and (**f**) 50°C. The images recorded using a dose of 6.67 e/Å^2/s were processed using a Python script for contrast enhancement and visibility. Insets in (**a–c**) show the background color variation around a representative crystal marked with white circles in (**a–c**).

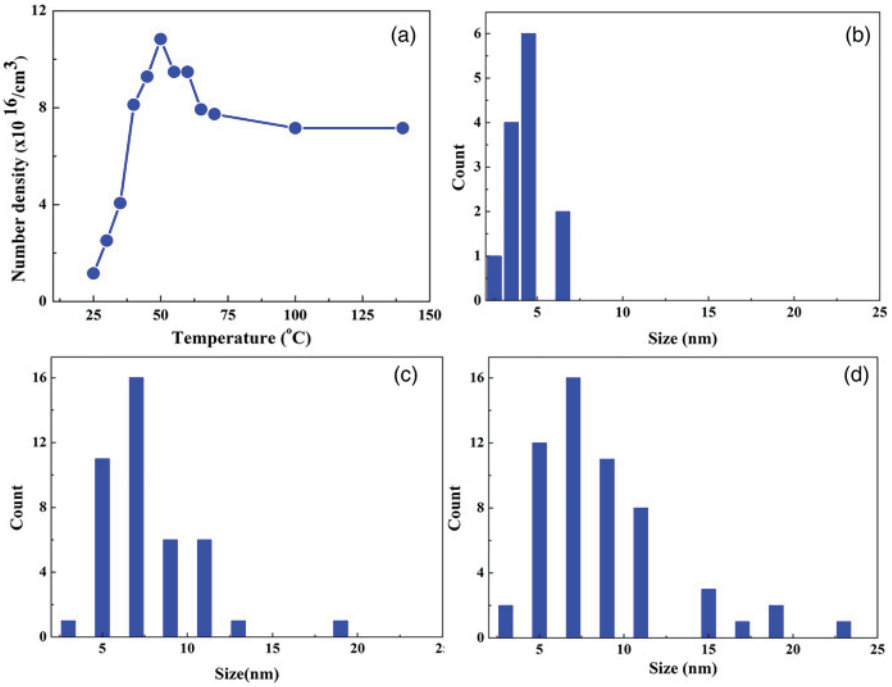

Fig. 5. Variation of number density of crystallites with respect to temperature (**a**). The size distribution histograms at 30, 40, and 50°C, respectively, derived from the processed images (**b–d**).

However, the presence of short-range order (SRO) and medium-range order (MRO) can also be one of the controlling factors of intensity in the power spectra series. Fluctuation electron microscopy (FEM) could be a suitable method to investigate this further. FEM is used to probe the MRO (0.5–2 nm) at nanometric scale in glasses and amorphous materials (Treacy & Gibson, 1996; Voyles & Muller, 2002). With this technique, a set of nano-beam, diffraction (NBD) patterns is collected at each probe position, while the sample is scanned by a fine probe. In contrast to long-range order (LRO) in materials, in the case of MRO, well-defined Bragg reflections are absent in the NBD patterns. The detection of MRO relies on the statistical examination of the speckle in the patterns (Rezikyan & Moore, 2020). FEM has been employed to reveal structural order at the nanoscale in melt-quenched amorphous GST-225 (Kwon et al., 2007). It has also been reported that melt-quenched amorphous GST-225 contains larger nuclei compared with its as-deposited counterpart (Lee et al., 2014). If the beam sensitivity can be overcome, FEM may become complementary to the present technique and 4D-STEM. The possible SRO and MRO regions in the SiN_x support of the Protochips heating chip may also give rise to these fine-colored dots.

Quantitative information on the nuclei number density and the crystallite size distribution at different temperatures is deduced from the Python-processed images and presented in Figures 5a–5d. The number density of the nuclei as a function of temperature is shown in Figure 5a whereas Figures 5b–5d depict the size distribution of the crystallites at 30, 40, and 50°C, respectively. The number density of the nuclei increases initially up to 50°C and saturates thereafter with further increase in temperature. This observation also supports the proposed process of nucleation-driven crystallization in GST-225 films. The size distribution of the crystallites at 30°C is narrow, with a median size of ~5 nm; the median shifts to ~7 nm for 40 and 50°C. The nature of the distribution is similar for both the 40 and 50°C curves; however, at 50°C, the number of crystallites at higher size range (≥10 nm) increases significantly more than its counterpart at 40°C.

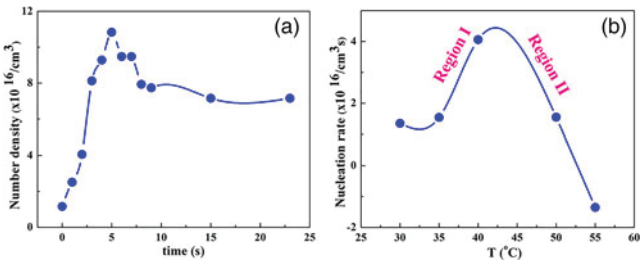

Fig. 6. Variation of number density of crystallites with respect to time (**a**). Plot of nucleation rate as a function of temperature (**b**).

Figure 6a shows the variation of nucleation density as a function of time. The nucleation rate versus temperature plot is displayed in Figure 6b. These plots confirm the higher nucleation rate at lower temperature (~42°C). This temperature is indeed lower compared with the existing reports, where the classical nucleation rate for GST-225 is a maximum at ~270°C (Orava & Greer, 2017). The observed lower temperature in the present study can be associated to surface crystallization owing to the presence of a greater number of heterogeneous nucleation sites. As mentioned above, the heterogeneous nucleation is favored by surface oxidation and the island morphology of the film. At lower temperatures, the crystallization is dominated by heterogeneous nucleation; however, the growth of the nucleated crystals is slow (region I in Fig. 6b). At higher temperatures (see region II in Fig. 6b), the accelerated growth kinetics leads to larger sizes of already nucleated crystals, in addition to the newly nucleated, smaller crystals.

Recently, the 4D-STEM technique has been developed as a tool to study relative orientations while imaging nanoparticles at a

low-dose; secondary phases in a glass matrix, polymers, and different beam-sensitive materials can also be studied (Bustillo et al., 2016; Ophus, 2019; Panova et al., 2019; Pekin et al., 2019; DeRocher et al., 2020). In this process, while scanning in the STEM mode, CBED information can also be recorded from each pixel. The recorded CBED patterns may be further processed to obtain the relative orientation map of the ROI. The approach adapted in the present paper complements the 4D-STEM methodology, where pseudo-orientation maps have been generated. In the present investigation, HRTEM images from an extremely beam-sensitive sample have been recorded in a phase-contrast, aberration-corrected TEM, rather than a STEM. Following this, power spectra are generated from 128×128 px regions and further processed with Python scripting to obtain the relative orientation map.

This present approach has several advantages over 4D-STEM. For *in situ* experiments like this one, the temporal resolution of 4D-STEM is still somewhat limited. To acquire 4D-STEM maps, the size of the maps shown in Figure 3, over 20,000 diffraction patterns, must be acquired. Using the same K3 IS camera, which can collect diffraction patterns at up to 3,858 FPS, this would take over 5 s. Each frame in the raw data shown here was captured in just 0.05 s. To increase the signal-to-noise in the final maps, three maps were summed together, resulting in one map every 0.15 s. This represents a data collection rate of over 133,000 map pixels per second. While faster cameras in the future will increase the speed at which 4D-STEM data can be collected, TEM cameras are also improving, so it is likely that TEM-based techniques like this one will always be capable of better temporal resolution. For researchers using an image-corrected TEM rather than a probe-corrected STEM, the microscope may produce better results in imaging mode, though the microscopist's familiarity with HRTEM versus STEM imaging may be an influencing factor.

The current computational scheme with Python scripting to process HRTEM micrographs can be a complementary technique to 4D-STEM to generate orientation maps from specimens that are extremely beam sensitive. This technique can also be adapted to probe the early stages of nucleation which is inherently unstable under the electron beam. In the present specimen, during early stages of crystallization, the crystallites are smaller than the thickness of the specimen. In this situation, the 4D-STEM process may impose a significant amount of beam damage and can alter how the material behaves. However, the HRTEM imaging in the phase-contrast mode can be obtained in a low-dose condition with a large-field-of-view camera. The acquired micrographs can be subsequently processed with Python scripting to generate similar orientation maps *vis-à-vis* that of 4D-STEM. The present approach is thus ideal for orientation mapping if the aberration-corrected TEM used is image-corrected, not probe-corrected.

Conclusions

The structural transformation in GST-225 at the early stages is observed with a low electron-dose, high-speed, large-field-of-view, direct-detection camera. The contrast enhancement and visibility in the recorded micrographs with low SNR has been achieved through Python scripting in the Digital Micrograph platform. This process enables quantitative analysis of the contrast in recorded micrographs which is otherwise barely visible. The current approach has the potential to be extended to investigate the early stages of phase-transformation events, nucleation and growth of low-dimensional materials from precursors, and for other beam-sensitive materials.

Acknowledgments. This research is supported by NSF under award DMR-1710468. The TEM studies were carried out at the Center for Integrated Nanotechnologies, an Office of Science User Facility operated for the U.S. Department of Energy (DOE) Office of Science, Sandia National Laboratories. The GST films were deposited at the Institute of Materials Science and Nanotechnology (UNAM) at Bilkent University, Turkey. The authors thank Drs. Helena Silva, Paul G. Kotula, Shalini Tripathi, John Watt, Gokhan Bakan, Matthew T. Janish, and Ali Gokirmak for helpful discussions. The use of the K3 IS camera was provided courtesy of Gatan. The Sandia National Laboratories are managed and operated by National Technology and Engineering Solutions of Sandia, LLC., a wholly owned subsidiary of Honeywell International, Inc., for the U.S. DOE's NNSA under contract DE-NA-0003525. The views expressed here do not necessarily represent the views of the U.S. DOE or the U.S. Government.

Conflict of interest. There are no conflicts to declare.

References

Bustillo KC, Panova O, Gammer C, Trigg EB, Chen XC, Yan L, Balsara NP, Winey KI & Minor AM (2016). Development of diffraction scanning techniques for beam sensitive polymers. *Microsc Microanal* **22**(S3), 492–493.

Carter CB & Williams DB (2016). *Transmission Electron Microscopy: Diffraction, Imaging, and Spectrometry*. Switzerland: Springer International Publishing.

Choi Y, Jung M & Lee Y-K (2009). Effect of heating rate on the activation energy for crystallization of amorphous $Ge_2Sb_2Te_5$ thin film. *Electrochem Solid State Lett* **12**(7), F17.

DeRocher KA, Smeets PJ, Goodge BH, Zachman MJ, Balachandran PV, Stegbauer L, Cohen MJ, Gordon LM, Rondinelli JM & Kourkoutis LF (2020). Chemical gradients in human enamel crystallites. *Nature* **583** (7814), 66–71.

Gao WP, Tieu P, Addiego C, Ma YL, Wu JB & Pan XQ (2019). Probing the dynamics of nanoparticle formation from a precursor at atomic resolution. *Sci Adv* **5**, 1.

Jiang T-T, Wang J-J, Lu L, Ma C-S, Zhang D-L, Rao F, Jia C-L & Zhang W (2019). Progressive amorphization of GeSbTe phase-change material under electron beam irradiation. *APL Mater* **7**(8), 081121.

Jiang T-T, Wang X-D, Wang J-J, Zhou Y-X, Zhang D-L, Lu L, Jia C-L, Wuttig M, Mazzarello R & Zhang W (2020). *In situ* study of vacancy disordering in crystalline phase-change materials under electron beam irradiation. *Acta Mater* **187**, 103–111.

Kooi B, Groot W & De Hosson JTM (2004). *In situ* transmission electron microscopy study of the crystallization of $Ge_2Sb_2Te_5$. *J Appl Phys* **95**(3), 924–932.

Kwon MH, Lee BS, Bogle SN, Nittala LN, Bishop SG, Abelson JR, Raoux S, Cheong BK & Kim KB (2007). Nanometer-scale order in amorphous $Ge_2Sb_2Te_5$ analyzed by fluctuation electron microscopy. *Appl Phys Lett* **90**, 2.

Lee B-S, Shelby RM, Raoux S, Retter CT, Burr GW, Bogle SN, Darmawikarta K, Bishop SG & Abelson JR (2014). Nanoscale nuclei in phase change materials: Origin of different crystallization mechanisms of $Ge_2Sb_2Te_5$ and AgInSbTe. *J Appl Phys* **115**, 6.

Li JJ, Li YP, Li Q, Wang ZC & Deepak FL (2019). Atomic-scale dynamic observation reveals temperature-dependent multistep nucleation pathways in crystallization. *Nanoscale Horiz* **4**(6), 1302–1309.

McMullan G, Clark AT, Turchetta R & Faruqi AR (2009). Enhanced imaging in low dose electron microscopy using electron counting. *Ultramicroscopy* **109**(12), 1411–1416.

Miller B, Pakzad A & Mick S (2019). Real-time electron counting for continuous TEM imaging of sensitive samples. *Microsc Microanal* **25**(S2), 1718–1719.

Murthy AA, Stanev TK, dos Reis R, Hao SQ, Wolverton C, Stern NP & Dravid VP (2020). Direct visualization of electric-field-induced structural dynamics in monolayer transition metal dichalcogenides. *ACS Nano* **14**(2), 1569–1576.

Nam KW, Park SS, dos Reis R, Dravid VP, Kim H, Mirkin CA & Stoddart JF (2019). Conductive 2D metal-organic framework for high-performance

cathodes in aqueous rechargeable zinc batteries. *Nat Commun* **10 (1), 4948**.

Noé P, Sabbione C, Bernier N, Castellani N, Fillot F & Hippert F (2016). Impact of interfaces on scenario of crystallization of phase change materials. *Acta Mater* **110**, 142–148.

Ogata AF, Rakowski AM, Carpenter BP, Fishman DA, Merham JG, Hurst PJ & Patterson JP (2020). Direct observation of amorphous precursor phases in the nucleation of protein-metal-organic frameworks. *J Am Chem Soc* **142**(3), 1433–1442.

Ophus C (2019). Four-dimensional scanning transmission electron microscopy (4D-STEM): From scanning nanodiffraction to ptychography and beyond. *Microsc Microanal* **25**(3), 563–582.

Orava J & Greer AL (2017). Classical-nucleation-theory analysis of priming in chalcogenide phase-change memory. *Acta Mater* **139**, 226–235.

Panova O, Ophus C, Takacs CJ, Bustillo KC, Balhorn L, Salleo A, Balsara N & Minor AM (2019). Diffraction imaging of nanocrystalline structures in organic semiconductor molecular thin films. *Nat Mater* **18**(8), 860–865.

Pekin TC, Ding J, Gammer C, Ozdol B, Ophus C, Asta M, Ritchie RO & Minor AM (2019). Direct measurement of nanostructural change during *in situ* deformation of a bulk metallic glass. *Nat Commun* **10**(1), 1–7.

Raoux S (2009). Phase change materials. *Annu Rev Mater Res* **39**, 25–48.

Rezikyan A & Moore GG (2020). Fluctuation electron microscopy study of crystal nucleation in TiO_2-SiO_2 glass with heat treatment. *J Phys Condens Matter* **32**(48), 485402.

Simpson R, Krbal M, Fons P, Kolobov A, Tominaga J, Uruga T & Tanida H (2010). Toward the ultimate limit of phase change in $Ge_2Sb_2Te_5$. *Nano Lett* **10**(2), 414–419.

Song SA, Zhang W, Sik Jeong H, Kim JG & Kim YJ (2008). *In situ* dynamic HR-TEM and EELS study on phase transitions of $Ge_2Sb_2Te_5$ chalcogenides. *Ultramicroscopy* **108**(11), 1408–1419.

Treacy M & Gibson J (1996). Variable coherence microscopy: A rich source of structural information from disordered materials. *Acta Crystallogr Sect A* **52** (2), 212–220.

Tripathi S, Janish M, Dirisaglik F, Cywar A, Zhu Y, Jungjohann K, Silva H & Carter CB (2018). Phase-change materials; the challenges for TEM. *Microsc Microanal* **24**(S1), 1904–1905.

Tripathi S, Kotula P, Singh MK, Ghosh C, Bakan G, Silva H & Carter CB (2020). Role of oxygen on chemical segregation in uncapped $Ge_2Sb_2Te_5$ thin films on silicon nitride. *ECS J Solid State Sci Technol* **9**(5), 054007.

Voyles P & Muller D (2002). Fluctuation microscopy in the STEM. *Ultramicroscopy* **93**(2), 147–159.

Wuttig M & Yamada N (2007). Phase-change materials for rewriteable data storage. *Nat Mater* **6**(11), 824–832.

Yamada N, Ohno E, Nishiuchi K, Akahira N & Takao M (1991). Rapid-phase transitions of GeTe-Sb_2Te_3 pseudobinary amorphous thin films for an optical disk memory. *J Appl Phys* **69**(5), 2849–2856.

Zhang DL, Zhu YH, Liu LM, Ying XR, Hsiung CE, Sougrat R, Li K & Han Y (2018). Atomic-resolution transmission electron microscopy of electron beam-sensitive crystalline materials. *Science* **359**(6376), 675–679.

Zhu YH, Ciston J, Zheng B, Miao XH, Czarnik C, Pan YC, Sougrat R, Lai ZP, Hsiung CE, Yao KX, Pinnau I, Pan M & Han Y (2017). Unravelling surface and interfacial structures of a metal-organic framework by transmission electron microscopy. *Nat Mater* **16**(5), 532–536.